

Analysis of thick functionally graded plates by using higher-order shear and normal deformable plate theory and MLPG method with radial basis functions

D.F. Gilhooley^{a,e,g}, R.C. Batra^d, J.R. Xiao^{a,*}, M.A. McCarthy^{e,f,g}, J.W. Gillespie Jr.^{a,b,c}

^a Center for Composite Materials, University of Delaware, Newark, DE 19716, USA

^b Department of Materials Science and Engineering, University of Delaware, Newark, DE 19716, USA

^c Department of Civil and Structural Engineering, University of Delaware, Newark, DE 19716, USA

^d Department of Engineering Science and Mechanics, Virginia Polytechnic Institute and State University, Blacksburg, VA 24061, USA

^e Composites Research Centre, University of Limerick, Ireland

^f Materials and Surface Science Institute, University of Limerick, Ireland

^g Department of Mechanical and Aeronautical Engineering, University of Limerick, Ireland

Available online 12 September 2006

Abstract

Infinitesimal deformations of a functionally graded thick elastic plate are analyzed by using a meshless local Petrov–Galerkin (MLPG) method, and a higher-order shear and normal deformable plate theory (HOSNDPT). Two types of Radial basis functions RBFs, i.e. Multiquadrics and Thin Plate Splines, are employed for constructing the trial solutions, while a fourth-order Spline function is used as the weight/test function over a local subdomain. Effective material moduli of the plate, made of two isotropic constituents with volume contents varying only in the thickness direction, are computed using the Mori–Tanaka homogenization technique. Computed results for a simply supported aluminum/ceramic plate are found to agree well with those obtained analytically. Results for a plate with two opposite edges free and the other two simply supported agree very well with those obtained by analyzing three-dimensional deformations of the plate by the finite element method. The distributions of the deflection and stresses through the plate thickness are also presented for different boundary conditions. It is found that both types of basis functions give accurate values of plate deflection, but the multiquadrics give better values of stresses than the thin plate splines.

© 2006 Elsevier Ltd. All rights reserved.

Keywords: Higher-order shear and normal deformable plate theory; Thick plate; Functionally graded materials; MLPG method; Radial basis function

1. Introduction

Functionally graded materials (FGMs) are a new generation of composite materials wherein the material properties vary continuously to yield a predetermined composition profile. These materials have been introduced to benefit from the ideal performance of its constituents, e.g. high heat/corrosion resistance of ceramics on one side, and large mechanical strength and toughness of metals on

the other side. FGMs have no interfaces and are hence advantageous over conventional laminated composites. FGMs also permit tailoring of material composition to optimize a desired characteristic such as minimize the maximum deflection for a given load and boundary conditions, or maximize the first frequency of free vibration, or minimize the maximum principal tensile stress. As a result, FGMs have gained potential applications in a wide variety of engineering components or systems, which include armor plating, heat engine components and human implants.

The variation of material properties in an FGM is usually achieved by continuously varying volume fractions of the constituent materials. FGMs with material properties

* Corresponding author. Tel.: +1 302 831 6109; fax: +1 302 831 8525.
E-mail address: xiao@ccm.udel.edu (J.R. Xiao).

varying only in the thickness direction can be manufactured by high-speed centrifugal casting [1,2], or by depositing ceramic layers on a metallic substrate [3,4]. An FGM with properties changing in the plane of a sheet can be produced by ultraviolet irradiation to alter the chemical composition [5]. A directed oxidation technique has also been employed [6,7] to deposit a ceramic layer on the outside surfaces of a structure. FG fiber reinforced composites can be fabricated by varying the volume fraction of fibers and/or their orientation in the preform prior to infusing resin into it. Commercially developed FGMs are available for use as structural elements in different applications. Here, we study static deformations of thick FG elastic plates.

A number of plate theories are available to analyze deformations of composite plates. The classical Kirchhoff plate theory ignores transverse shear effects, provides reasonable results for relatively thin plates, and suffices for computing the first few modes of flexural vibrations. However, it may not give good values of higher modes of flexural vibration for moderately thick plates (thickness/span $> 1/10$) and does not give through-the-thickness modes of vibration of very thick plates. Some shortcomings of the Kirchhoff plate theory are remedied by a number of shear deformable plate theories the simplest of which is the first-order shear deformation theory (Reissner–Mindlin theory), which assumes constant transverse shear strain in the thickness direction and requires a shear correction factor to account for the deviation of the actual transverse shear strain from the constant one. The value of the shear correction factor depends on geometric parameters, applied loads and boundary conditions. Second and higher-order shear deformation plate theories [8–11] use higher-order polynomials in the expansion of displacement components along the plate's thickness, and require no shear correction factors. First- and third-order shear deformation theories coupled with the finite element method (FEM) have been used by several authors [12–16] to analyze deformations of FG plates. The higher-order shear and normal deformable plate theory (HOSNDPT) developed by Batra and coworkers [10,17] has the following advantages: it accounts for both transverse normal and transverse shear deformations, it exactly satisfies traction boundary conditions prescribed on plate's major surfaces, the governing equations are second-order partial differential equations enabling the use of Lagrange shape functions in the FEM, transverse stresses are computed from plate equations rather than by integrating the balance of linear momentum in the thickness direction and the in-plane stresses computed from the plate equations, and it can accurately predict through-the-thickness modes of vibration which correspond to null lateral displacements or deflections. The plate theory is called compatible if stresses are derived from the assumed displacement field and Hooke's law, and mixed if stresses and displacements are expanded independently through the plate thickness. The mixed theory, originally devel-

oped for piezoelectric plates, has been used for studying the propagation of plane waves, free vibrations of thick homogeneous isotropic and transversely isotropic plates [17,18]; and the compatible theory for static and dynamic deformations of isotropic homogeneous [19] and FG thick plates [20], and transient thermomechanical deformations of a FG plate [21].

Approximate solutions of complex engineering problems are usually obtained by a numerical method. Meshless methods such as the Element-Free Galerkin (EFG) method [22], the Reproducing Kernel Particle Method (RKPM) [23], hp-clouds [24], the Partition of Unity Method (PUM) [25], and the Meshless Local Petrov–Galerkin (MLPG) method [26,27] have attracted considerable attention recently. Among these, the MLPG method does not need any mesh for either generating basis functions for the trial solution and the test function or numerical integration of integrals appearing in the weak formulation of the problem. Six MLPG formulations for different choices of test functions have been labelled MLPG1 – MLPG6 in [27]. The basis functions for the trial solution and/or the test functions can be generated by either the Moving Least Squares (MLS) approximation, or the PUM, or the Shepard functions, or the RKPM; however, these are generally rational functions, and lack the Kronecker delta function property. Thus special techniques, such as the use of penalty parameters or Lagrange multipliers, are needed to satisfy essential (e.g., displacement type) boundary conditions.

Static and transient infinitesimal deformations of thick FG elastic plates using Batra and Vidoli's plate theory have been analyzed with the MLPG method and basis functions derived by the MLS approximation [19–21]. The matrix transformation technique, used to impose essential boundary conditions, considerably increased the computational cost. Recently, Radial Basis Functions (RBFs) [28] have been employed to solve partial differential equations [29–31], and to approximate the trial solution in meshless methods [32–36]; RBFs have the Kronecker delta property, which facilitates satisfying the essential boundary conditions. Furthermore, when RBFs are used in the weak formulation of a problem over a local domain (such as in an MLPG method [34–36]) rather than over a global domain, the dense system matrices associated with the global interpolation are avoided. The extended Multiquadrics (MQ), $g(r) = (r^2 + c^2)^\beta$, and the Thin Plate Splines (TPS) have been successfully employed in the MLPG formulation in [36] for the solution of two-dimensional problems where the TPS were modified to $g(r) = r^\alpha \log r$ with α taken as a shape parameter. Here r is the distance between two points, and c and β are constants.

The analysis of thick FG plates with the compatible HOSNDPT and the MLPG method is presented in [20] where the MLS approximation was used to generate basis functions for the trial solution. The meshless collocation method [37], the MQ radial basis functions and a third-order shear deformation theory have been used to analyze

static deformations of functionally graded square plates. Here we use the RBFs, an MLPG method, and the compatible HOSNDPT to analyze deformations of a thick FG plate. Either the MQ or the TPS are employed as basis functions for the trial solution, and a fourth-order spline weighting function is used as the test function; such an approach is called MLPG1 in [27]. Material properties, taken to vary in the thickness direction only, are determined with the Mori–Tanaka homogenization scheme [38]. Results for a simply supported aluminum/ceramic FG plate are compared with the analytical solution of Vel and Batra [39]. The distributions of displacements and stresses through the plate thickness are presented for different boundary conditions. The effect of varying the volume fraction of Zirconia on the plate’s top surface on plate’s deformations is also examined.

2. Review of the compatible higher-order shear and normal deformable plate theory (HOSNDPT)

A rectangular Cartesian coordinate system, shown in Fig. 1, is used to describe infinitesimal deformations of a rectangular plate occupying the region Ω defined by $0 \leq x \leq a, 0 \leq y \leq b$, and $-t/2 \leq z \leq t/2$. The mid-surface, $z = 0$, of the plate is denoted by S , and displacements of a point along the x -, the y - and the z -axes by u , v , and w , respectively. Displacements are expanded in the thickness (z -) direction in terms of Legendre polynomials orthonormalized by

$$\int_{-t/2}^{t/2} L_i(z)L_j(z)dz = \delta_{ij}, \quad i, j = 0, 1, 2, \dots, \quad (1)$$

where δ_{ij} is the Kronecker delta and $L_i(z)$ is the i th Legendre polynomial. Orthonormal Legendre polynomials are equivalent to the basis $1, z, z^2, \dots$, and have the advantage of reducing the algebraic work. Expressions for the first seven orthonormal Legendre polynomials are:

$$L_0(z) = \frac{1}{\sqrt{t}}, \quad L_1(z) = 2\sqrt{\frac{3z}{t}}, \quad (2a)$$

$$L_2(z) = \frac{1}{2}\sqrt{\frac{5}{t}}\left[12\left(\frac{z}{t}\right)^2 - 1\right], \quad (2b)$$

$$L_3(z) = \sqrt{\frac{7}{t}}\left[-3\left(\frac{z}{t}\right) + 20\left(\frac{z}{t}\right)^3\right], \quad (2c)$$

$$L_4(z) = \frac{3}{\sqrt{t}}\left[\frac{3}{8} - 15\left(\frac{z}{t}\right)^2 + 70\left(\frac{z}{t}\right)^4\right], \quad (2d)$$

$$L_5(z) = \sqrt{\frac{11}{t}}\left[\frac{15}{4}\left(\frac{z}{t}\right) - 70\left(\frac{z}{t}\right)^3 + 252\left(\frac{z}{t}\right)^5\right], \quad (2e)$$

$$L_6(z) = \sqrt{\frac{13}{t}}\left[-\frac{5}{16} + \frac{105}{4}\left(\frac{z}{t}\right)^2 - 315\left(\frac{z}{t}\right)^4 + 924\left(\frac{z}{t}\right)^6\right], \quad (2f)$$

$$L_7(z) = \sqrt{\frac{15}{t}}\left[-\frac{35}{8}\left(\frac{z}{t}\right) + \frac{315}{2}\left(\frac{z}{t}\right)^3 - 1386\left(\frac{z}{t}\right)^5 + 3432\left(\frac{z}{t}\right)^7\right]. \quad (2g)$$

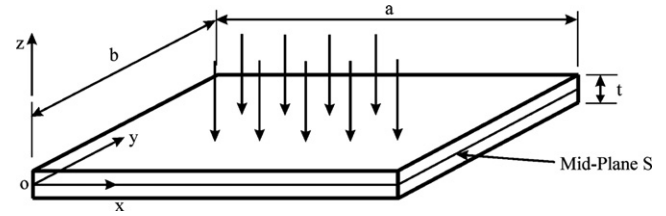


Fig. 1. A schematic sketch of the problem studied.

We set

$$\mathbf{u} = \begin{Bmatrix} u(x, y, z) \\ v(x, y, z) \\ w(x, y, z) \end{Bmatrix} = \sum_{i=0}^K \begin{Bmatrix} u_i(x, y) \\ v_i(x, y) \\ w_i(x, y) \end{Bmatrix} L_i(z), \quad (3)$$

where K is the order of the plate theory; for $K \leq 2$, the plate theory is called higher order. It should be noted that $u_i, v_i, w_i (i = 0, 1, 2, \dots, K)$ have the units of $(\text{length})^{1/2}$ since dimensions of orthonormal Legendre polynomials are $1/(\text{length})^{1/2}$. Recalling that $L'_i(z) = dL_i/dz$ is a polynomial of degree $(i - 1)$ in z , we write

$$L'_i(z) = \sum_{j=0}^K d_{ij}L_j(z), \quad (4)$$

where d_{ij} are constants. For $K = 7$,

$$d_{ij} = \begin{bmatrix} 0 & 0 & 0 & 0 & 0 & 0 & 0 & 0 \\ \sqrt{3} & 0 & 0 & 0 & 0 & 0 & 0 & 0 \\ 0 & \sqrt{15} & 0 & 0 & 0 & 0 & 0 & 0 \\ \sqrt{7} & 0 & \sqrt{35} & 0 & 0 & 0 & 0 & 0 \\ 0 & 3\sqrt{3} & 0 & 3\sqrt{7} & 0 & 0 & 0 & 0 \\ \sqrt{11} & 0 & \sqrt{55} & 0 & 3\sqrt{11} & 0 & 0 & 0 \\ 0 & \sqrt{39} & 0 & \sqrt{91} & 0 & \sqrt{143} & 0 & 0 \\ \sqrt{15} & 0 & 5\sqrt{3} & 0 & 3\sqrt{15} & 0 & \sqrt{195} & 0 \end{bmatrix}. \quad (5)$$

Note that elements in the first row and the last column of the $(K + 1) \times (K + 1)$ matrix d_{ij} are zeros. For infinitesimal deformations, the strains ε are given by

$$\varepsilon = \begin{Bmatrix} \varepsilon_{xx} \\ \varepsilon_{yy} \\ \varepsilon_{zz} \\ 2\varepsilon_{yz} \\ 2\varepsilon_{zx} \\ 2\varepsilon_{xy} \end{Bmatrix} = \sum_{i=0}^K \begin{Bmatrix} \frac{\partial u_i(x, y)}{\partial x} \\ \frac{\partial v_i(x, y)}{\partial y} \\ \sum_{j=0}^K w_j(x, y)d_{ji} \\ \frac{\partial w_i(x, y)}{\partial y} + \sum_{j=0}^K v_j(x, y)d_{ji} \\ \frac{\partial w_i(x, y)}{\partial x} + \sum_{j=0}^K u_j(x, y)d_{ji} \\ \frac{\partial v_i(x, y)}{\partial x} + \frac{\partial u_i(x, y)}{\partial y} \end{Bmatrix} L_i(z) \equiv \sum_{i=0}^K \{\eta_i\} L_i(z), \quad (6)$$

where for $i = 0, 1, 2, \dots, K$, η_i is a six-dimensional vector with components

$$\eta_{i(1)} = \partial u_i / \partial x, \quad \eta_{i(2)} = \partial v_i / \partial y, \quad \eta_{i(3)} = \sum_{j=0}^K d_{ji} w_j, \quad (7a)$$

$$\eta_{i(4)} = \partial w_i / \partial y + \sum_{j=0}^K v_j d_{ji}, \quad \eta_{i(5)} = \partial w_i / \partial x + \sum_{j=0}^K u_j d_{ji}, \quad (7b)$$

$$\eta_{i(6)} = \partial v_i / \partial x + \partial u_i / \partial y. \quad (7c)$$

The terms involving d_{ij} couple K th order displacements with those of lower order. Using Hooke's law, stresses at a material point $\mathbf{x} = (x, y, z)$ are given by

$$\boldsymbol{\sigma} = \{ \sigma_{xx} \quad \sigma_{yy} \quad \sigma_{zz} \quad \sigma_{yz} \quad \sigma_{zx} \quad \sigma_{xy} \}^T = \mathbf{D}\boldsymbol{\varepsilon}, \quad (8)$$

where \mathbf{D} , the matrix of elastic constants, is a function of z . Substitution from (6) and (7) into (8) gives stresses at a point (x, y, z) in terms of displacements and in-plane gradients of displacements at the point $(x, y, 0)$.

Let \tilde{u} , \tilde{v} , and \tilde{w} be three linearly independent functions defined on the mid-surface S . Multiplying equations expressing the balance of linear momentum in the x -, the y -, and z -directions by \tilde{u} , \tilde{v} , and \tilde{w} , respectively, adding the resulting equations, and using the divergence theorem, we obtain

$$\int_{\Omega} \tilde{\boldsymbol{\varepsilon}}^T \boldsymbol{\sigma} \, d\Omega - \int_{\Gamma_u} \tilde{\mathbf{u}}^T \boldsymbol{\sigma} \mathbf{n} \, d\Gamma - \int_{\Omega} \tilde{u} f \, d\Omega - \int_{\Gamma_f} \tilde{\mathbf{u}}^T \bar{\mathbf{f}} \, d\Gamma - \int_S \tilde{\mathbf{u}}^T \mathbf{q}^{\pm} \, dS = 0, \quad (9)$$

where \mathbf{n} is the unit outward normal on the boundary $\partial\Omega$, f the body force, $\tilde{\boldsymbol{\varepsilon}}$ the strain vector obtained from Eq. (6) with u , v , and w replaced by \tilde{u} , \tilde{v} , and \tilde{w} , respectively, $\{\mathbf{q}^{\pm}\}$ the traction on the top and the bottom surfaces of the plate, Γ_u and Γ_f are disjoint parts of the boundary Γ of S where displacements and surface tractions are prescribed, respectively, as $\bar{\mathbf{u}}$ and $\bar{\mathbf{f}}$. Neglecting the body force, substituting from (6) and (8) into (9), and integrating with respect to z from $-t/2$ to $t/2$ give

$$\sum_{i=0}^K \sum_{j=0}^K \left[\int_S \{\tilde{\eta}_i\}^T [D_{ij}] \{\eta_j\} \, dS - \int_{\Gamma_u} \{\tilde{\eta}_i\}^T [n] [D_{ij}] \{\eta_j\} \, dS \right] = \sum_{i=0}^K \left[\int_{\Gamma_f} \{\tilde{u}_i\}^T \{\bar{f}_i\} \, d\Gamma + L_i \left(\pm \frac{t}{2} \right) \int_S \{\tilde{u}_i\}^T \{\mathbf{q}^{\pm}\} \, dS \right] \quad (10)$$

where

$$\{\bar{f}_i\} = \int_{-t/2}^{t/2} L_i(z) \{f\} \, dz, \quad (11a)$$

$$[D_{ij}] = \int_{-t/2}^{t/2} [D] L_i(z) L_j(z) \, dz \quad (11b)$$

and the matrix $[D_{ij}]$ is $6(K+1) \times 6(K+1)$. Since material properties are assumed to vary in the thickness direction only, D_{ij} is independent of x and y . For a plate made of a homogeneous material, Eq. (11b) simplifies to $[D_{ij}] = [D] \delta_{ij}$.

3. Interpolation using radial basis functions

Consider a continuous function $u(x)$ defined on the domain Ω having a set of nodes suitably located in it. Using polynomial and radial basis functions, an interpolation of $u(\mathbf{x})$ in terms of quantities evaluated at nodes surrounding a point \mathbf{x}_Q can be written as

$$u(\mathbf{x}, \mathbf{x}_Q) = \sum_{i=1}^n g_i(\mathbf{x}) a_i(\mathbf{x}_Q) + \sum_{j=1}^m p_j(\mathbf{x}) b_j(\mathbf{x}_Q), \quad (12)$$

$$\sum_{i=1}^n p_j(x_i, y_i) a_i = 0, \quad j = 1, 2, \dots, m, \quad (13)$$

where n is the number of nodes in the neighborhood of \mathbf{x}_Q , $g_i(\mathbf{x})$ the radial basis function, $p_j(\mathbf{x})$ the monomial, $m \ll n$ the number of polynomial terms, and $a_i(\mathbf{x}_Q)$ and $b_j(\mathbf{x}_Q)$ are coefficients to be determined.

Enforcing the interpolation to pass through all n scattered points within the domain of influence leads to

$$A \begin{Bmatrix} a \\ b \end{Bmatrix} = \begin{bmatrix} G_0 & P_0 \\ P_0^T & 0 \end{bmatrix} \begin{Bmatrix} a \\ b \end{Bmatrix} = \begin{Bmatrix} u^e \\ 0 \end{Bmatrix}, \quad (14)$$

where

$$u^e = [u_1, u_2, u_3, \dots, u_n]^T, \quad (15)$$

$$G_0 = \begin{bmatrix} g_1(x_1, y_1) & g_2(x_1, y_1) & \cdots & g_n(x_1, y_1) \\ g_1(x_2, y_2) & g_2(x_2, y_2) & \cdots & g_n(x_2, y_2) \\ \vdots & \vdots & \ddots & \vdots \\ g_1(x_n, y_n) & g_2(x_n, y_n) & \cdots & g_n(x_n, y_n) \end{bmatrix}_{n \times n}, \quad (16)$$

$$P_0 = \begin{bmatrix} p_1(x_1, y_1) & p_2(x_1, y_1) & \cdots & p_m(x_1, y_1) \\ p_1(x_2, y_2) & p_2(x_2, y_2) & \cdots & p_m(x_2, y_2) \\ \vdots & \vdots & \ddots & \vdots \\ p_1(x_n, y_n) & p_2(x_n, y_n) & \cdots & p_m(x_n, y_n) \end{bmatrix}_{n \times m}. \quad (17)$$

The interpolation of the function $u(x)$ can then be expressed as

$$u(\mathbf{x}) = [G^T(\mathbf{x}) P^T(\mathbf{x})] A^{-1} \begin{Bmatrix} u^e \\ 0 \end{Bmatrix} = \Phi(\mathbf{x}) u^e, \quad (18)$$

where the shape function $\Phi(\mathbf{x})$ is given by

$$\Phi(\mathbf{x}) = [\phi_1(\mathbf{x}), \phi_2(\mathbf{x}), \phi_3(\mathbf{x}), \dots, \phi_k(\mathbf{x}), \dots, \phi_n(\mathbf{x})] \quad (19)$$

with

$$\phi_k(\mathbf{x}) = \sum_{i=1}^n g_i(\mathbf{x}) \bar{A}_{i,k} + \sum_{j=1}^m p_j(\mathbf{x}) \bar{A}_{n+j,k}. \quad (20)$$

Here $\bar{A}_{i,k}$ is the (i, k) element of the matrix A^{-1} . The derivatives of $\phi_k(\mathbf{x})$ have the following expressions:

$$\frac{\partial \phi_k}{\partial x} = \sum_{i=1}^n \frac{\partial g_i}{\partial x} \bar{A}_{i,k} + \sum_{j=1}^m \frac{\partial p_j}{\partial x} \bar{A}_{n+j,k}, \quad (21)$$

$$\frac{\partial \phi_k}{\partial y} = \sum_{i=1}^n \frac{\partial g_i}{\partial y} \bar{A}_{i,k} + \sum_{j=1}^m \frac{\partial p_j}{\partial y} \bar{A}_{n+j,k}. \quad (22)$$

Among the many choices for RBFs we use the following Multiquadrics (MQ) and Thin Plate Splines (TPS).

$$g_i(x, y) = (r_i^2 + c^2)^\beta, \quad (\text{MQ}) \quad (23a)$$

$$g_i(x, y) = (r_i)^2 \log r_i, \quad (\text{TPS}) \quad (23b)$$

Here, constants β , c , and α are shape parameters, and $r_i = [(x - x_i)^2 + (y - y_i)^2]^{1/2}$.

4. Implementation of the MLPG method for the compatible HOSNDPT

4.1. Test function of MLPG1

In the MLPG1 method employed here, the weight function is taken as the test function. That is

$$\psi_J = W(\mathbf{x} - \mathbf{x}_J). \quad (24)$$

Furthermore, we use the following fourth-order spline function as the weight function.

$$W(\mathbf{x} - \mathbf{x}_J) = \begin{cases} 1 - 6\left(\frac{d_J}{r_s}\right)^2 + 8\left(\frac{d_J}{r_s}\right)^3 - 3\left(\frac{d_J}{r_s}\right)^4, & 0 \leq d_J \leq r_s, \\ 0, & d_J \geq r_s. \end{cases} \quad (25)$$

Here $d_J = |\mathbf{x} - \mathbf{x}_J|$, and r_s equals the support of the weight function. We use circular subdomains of radius r_s centered at the node located at x_i , hereafter also called node I or x_i ; thus the support of W equals the subdomain.

4.2. Derivation of algebraic equations

Let $S_i \subset S$ be a smooth two-dimensional region associated with a node in S , $\Gamma_{ui} = \partial S_i \cup \Gamma_u$, $\Gamma_{fi} = \partial S_i \cup \Gamma_f$ and $\Gamma_{i0} = \partial S_i - \Gamma_{ui} - \Gamma_{fi}$. Let $\phi_1, \phi_2, \dots, \phi_N$, and $\psi_1, \psi_2, \dots, \psi_N$ be linearly independent functions defined on S_i . For a K th order plate theory there are $3(K + 1)$ unknowns at a point in S_i or S . We write these as a $3(K + 1)$ -dimensional array and set

$$\{u(x, y)\} = \sum_{J=1}^N [\phi_J(x, y)] \{\delta_J\}, \quad (26)$$

$$\{\tilde{u}(x, y)\} = \sum_{J=1}^N [\psi_J(x, y)] \{\tilde{\delta}_J\}, \quad (27)$$

where for each J , $\{\delta_J\}$ is a $3(K + 1)$ -dimensional array, and $[\phi_J]$ a square matrix of $3(K + 1)$ rows and columns. Similarly, $\{\tilde{\delta}_J\}$ is a $3(K + 1)$ -dimensional array, and $[\psi_J]$ a square matrix of $3(K + 1)$ rows and columns. The shape functions ϕ_J are obtained using the radial basis functions described above, and functions ψ_J equal the weight functions. The unknowns $\{\delta_J\}$ are nodal displacements (similar to those in the FEM). Substitution from (26) into (7) gives

$$\{\eta\} = \sum_{J=1}^N [B_J] \{\delta_J\}, \quad \{\tilde{\eta}\} = \sum_{J=1}^N [\tilde{B}_J] \{\tilde{\delta}_J\}, \quad (28)$$

where $\{\eta\}$ is a $6(K + 1)$ -dimensional array, and B_J a $6(K + 1) \times 3(K + 1)$ matrix. The $6(K + 1)$ rows of B_J can be divided into $(K + 1)$ blocks of six rows each. The six rows of the i th block of B_J are given below

$$\begin{bmatrix} \overbrace{0 \ 0 \ 0}^0 & \overbrace{\partial\phi_J/\partial x \ 0 \ 0}^i & \overbrace{0 \ 0 \ 0}^K \\ 0 \ 0 \ 0 & 0 \ \partial\phi_J/\partial y \ 0 & 0 \ 0 \ 0 \\ 0 \ 0 \ \phi_J d_{0i} & 0 \ 0 \ \phi_J d_{ii} & 0 \ 0 \ \phi_J d_{Ki} \\ 0 \ \phi_J d_{0i} \ 0 & 0 \ \phi_J d_{ii} \ \partial\phi_J/\partial y & 0 \ \phi_J d_{Ki} \ 0 \\ \phi_J d_{0i} \ 0 \ 0 & \phi_J d_{ii} \ 0 \ \partial\phi_J/\partial x & \phi_J d_{Ki} \ 0 \ 0 \\ 0 \ 0 \ 0 & \partial\phi_J/\partial y \ \partial\phi_J/\partial x \ 0 & 0 \ 0 \ 0 \end{bmatrix}. \quad (29)$$

Elements of matrix \tilde{B}_J are obtained from those of matrix B_J by replacing ϕ_J with ψ_J . Replacing the domain S of integration in Eq. (10) by S_i , substituting for $\{u\}$ and $\{\tilde{u}\}$ from Eqs. (26) and (27), and requiring that the resulting equation hold for all choices of $\{\tilde{\delta}\}$, we arrive at the following system of algebraic equations:

$$[K_{IJ}] \{\delta_J\} = \{F_I\}, \quad (30)$$

where

$$[K_{IJ}] = \int_{S_i} ([\tilde{B}_I]^T [D] [B_J]) d\Omega - \int_{\Gamma_{ui}} ([\psi_I]^T [n] [D] [B_J]) d\Gamma - \int_{\Gamma_{i0}} ([\psi_I]^T [n] [D] [B_J]) d\Gamma, \quad (31)$$

$$\{F_I\} = \int_{\Gamma_{fi}} [\psi_I]^T \{\tilde{f}\} d\Gamma + L_i(\pm t/2) \int_{S_i} [\psi_I]^T \{q^\pm\} d\Omega. \quad (32)$$

Equations similar to Eq. (30) are derived for each circular subdomain S_i with center at the node x_i . Gauss quadrature rule of an appropriate order is employed to numerically evaluate integrals over each subdomain. For each quadrature point, the trial solution is interpolated. Therefore, for a node x_i there are two local domains: the support of the test function which is a circle of radius r_s centered at x_i , and the interpolation domain of size r_i for each Gauss point. Fig. 2 shows the local subdomain for the node x_i , and the interpolation domain for the integration point \mathbf{x}_Q . These two domains are independent of each other, and we set $r_s = \alpha_s d_i$, and $r_i = \alpha_i d_i$, where α_s and α_i are constants, and d_i is the distance from the node x_i to the node nearest to it.

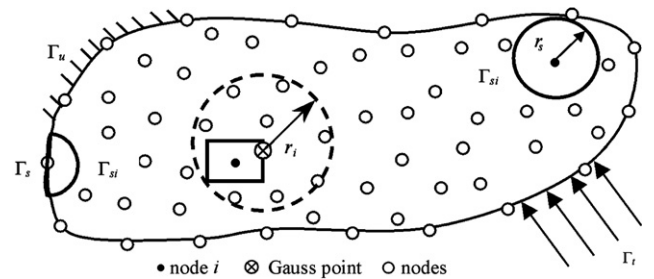


Fig. 2. The support and interpolation domains used in deriving discrete equations for node i ; the region enclosed by a solid circle of radius r_s equals the support of node i , and that enclosed by the dotted circle of radius r_i represents the interpolation domain.

5. Effective elastic moduli

Methods available to determine effective elastic moduli of a composite comprised of two constituents include the Rule of Mixtures, the three-phase model of Frohlich and Sack [40], the Self-Consistent scheme [41], the Mori–Tanaka technique [38], the mean field approach [42], and the representative volume element. With effective moduli determined by the Mori–Tanaka and the Self-Consistent methods, Vel and Batra [39,43,44] have given an analytical solution for static and dynamic deformations of a simply supported FG plate. Qian et al. [20] also used the Mori–Tanaka method to find effective elastic moduli, and then studied deformations of FG thick plates with the MLPG method. The rule of mixtures is the easiest to use but does not account for the interaction among constituents. The Mori–Tanaka method accounts approximately for these interactions, and is used here to determine the effective bulk modulus K_e and the effective shear modulus μ_e from the following relations:

$$\frac{K_e - K_1}{K_2 - K_1} = \frac{V_2}{1 + (1 - V_2)(3(K_2 - K_1)/(3K_1 + 4\mu_1))}, \tag{33}$$

$$\frac{\mu_e - \mu_1}{\mu_2 - \mu_1} = \frac{V_2}{1 + (1 - V_2)(\mu_2 - \mu_1)/(\mu_1 + \mu_1(9K_1 + 8\mu_1)/6(K_1 + 2\mu_1))}. \tag{34}$$

Here K_1 , μ_1 , and V_1 are, respectively, the bulk modulus, the shear modulus and the volume fraction of constituent 1, and K_2 , μ_2 and $V_2 = 1 - V_1$ are the corresponding quantities of constituent 2. The effective mass density of the homogenized medium is determined exactly by the rule of mixtures. The effective bulk and the shear moduli are related to Young’s modulus and Poisson’s ratio at each single point in through-thickness direction by

$$K = \frac{E}{3(1 - 2\nu)}, \quad \mu = \frac{E}{2(1 + \nu)}. \tag{35}$$

6. Numerical solution of problems

A number of problems have been analyzed to demonstrate the accuracy and the convergence of the present method. Boundary conditions imposed at a simply supported (S), a clamped (C), and a free (F) edge are

$$\begin{aligned} S: & \quad \sigma_{xx} = 0, \quad w = v = 0 \text{ on } x = 0, a, \\ & \quad \sigma_{yy} = 0, \quad u = w = 0 \text{ on } y = 0, b; \\ C: & \quad u = v = w = 0, \text{ on } x = 0, a; y = 0, b, \\ F: & \quad \sigma_{xx} = \sigma_{xy} = \sigma_{xz} = 0 \text{ on } x = 0, a; \\ & \quad \sigma_{yy} = \sigma_{yx} = \sigma_{yz} = 0 \text{ on } y = 0, b. \end{aligned}$$

FG plates are comprised of either an aluminum alloy (Al) and zirconia (ZrO_2) or an aluminum alloy and a ceramic (SiC). Values of parameters for these materials are

$$Al : E_m = 70 \text{ GPa}, \quad \nu_m = 0.3, \quad \rho_m = 2702 \text{ kg/m}^3$$

$$ZrO_2 : E_z = 200 \text{ GPa}, \quad \nu_z = 0.3, \quad \rho_z = 5700 \text{ kg/m}^3$$

$$SiC : E_c = 427 \text{ GPa}, \quad \nu_c = 0.17, \quad \rho_c = 3100 \text{ kg/m}^3$$

The volume fraction of the ceramic is given by

$$V_c = V_c^- + (V_c^+ - V_c^-) \left(\frac{1}{2} + \frac{z}{t} \right)^p, \tag{36}$$

where V_c^+ and V_c^- are, respectively, volume fractions of the ceramic on the top and the bottom surfaces of the plate, and the parameter p dictates the variation through the thickness of the volume fraction of the ceramic. For an aluminum/zirconia FG plate, $p = 0$ and ∞ correspond, respectively, to homogeneous plates with uniform distributions, V_c^+ and V_c^- , of zirconia. The through-the-thickness variation of the effective Young’s modulus, E , of the composite for different values of p is exhibited in

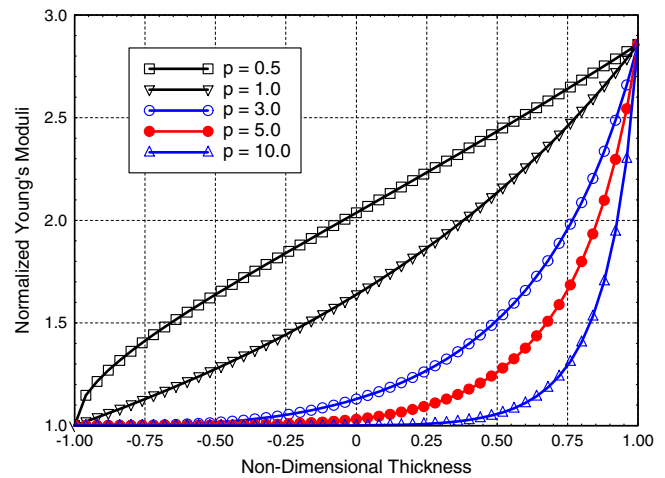


Fig. 3. For different values of p , variation of Young’s modulus through the plate thickness.

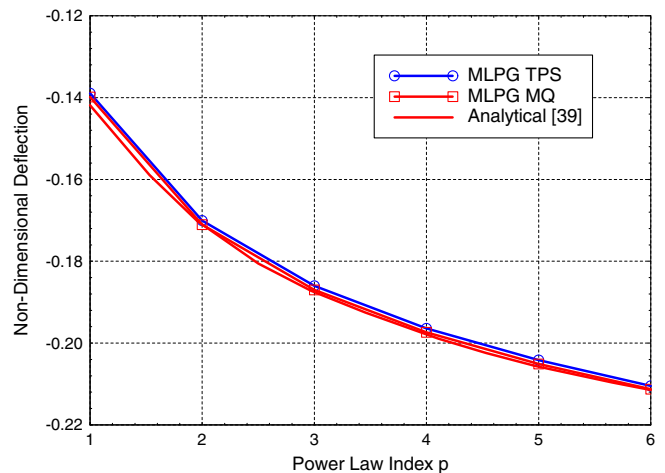


Fig. 4. Comparison of the computed non-dimensional centroidal deflection with that obtained from the analytical solution (SSSS square plate, pressure = $q_0 \sin \pi x/a \sin \pi y/a$, $V_c^- = 0$, $V_c^+ = 1$).

Fig. 3 for the aluminum/zirconia plate. Poisson’s ratio, computed from Eqs. (33)–(35) also varies through the plate thickness. The midsurface of the square plate is discretized with 169 uniformly distributed nodes. For all example problems studied, the fifth-order plate theory ($K = 5$) is used, and plate thickness/length equals 0.2; thus the plate is thick.

As indicated in [34–36], the selection of the shape parameters of RBFs affects the accuracy and performance of the meshless method for two-dimensional solid problems, and could be influenced by the ‘mesh’ size/density. The optimal values of the shape parameters obtained for the two-dimensional solid problems [34–36] may not be applicable to other engineering problems with different PDEs. The authors have conducted a systematic study on

the effect of the shape parameters on the bending analysis of thick isotropic homogeneous plates [45], and our previous results has indicated that optimum values of shape parameters for plate problems are the same as those for two-dimensional elasticity problems [36]. It was also found in [45] that for the Multiquadric RBFs, there is a wide range of values of the shape parameter c which yield acceptable results; optimum values of shape parameters are $c = 6d$, $\beta = 1.99$ for MQ, and $\alpha = 4$ for TPS where d is the minimum distance between any two nodes. These values should work for the FG plate too since two-dimensional equations for a FG plate differ from those of a homogeneous plate in the evaluation of the matrix $[D_{ij}]$ defined by Eq. (11b). An interesting aspect of the present work is to delineate through-the-thickness variation of dif-

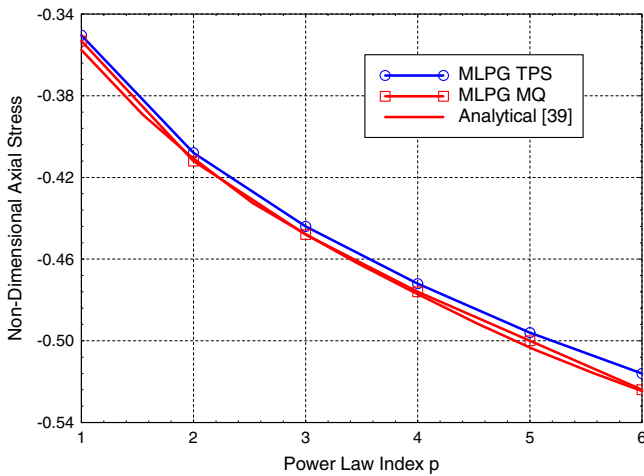


Fig. 5. Comparison of the computed non-dimensional axial stress at the center of the top surface with that obtained from the analytical solution (SSSS square plate, pressure = $q_0 \sin \pi x/a \sin \pi y/a$, $V_c^- = 0$, $V_c^+ = 1$).

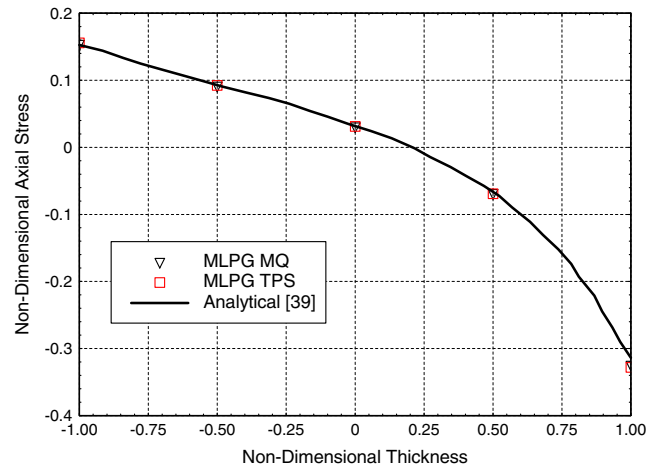


Fig. 7. Comparison of through-the-thickness variation of the computed axial stress at points on the vertical line passing through the plate centroid with that obtained from the analytical solution (SSSS square plate, pressure = $q_0 \sin \pi x/a \sin \pi y/a$, $V_c^- = 0$, $V_c^+ = 0.75$, $p = 2$).

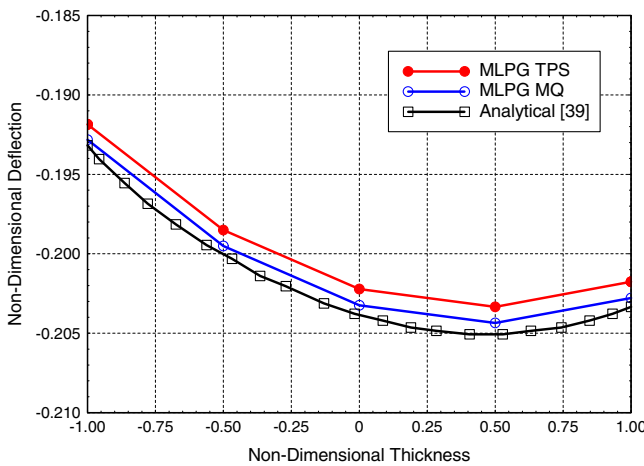


Fig. 6. Comparison of the computed deflection of points on the vertical line passing through the plate centroid with that derived from the analytical solution (SSSS square plate, pressure = $q_0 \sin \pi x/a \sin \pi y/a$, $V_c^- = 0$, $V_c^+ = 0.75$, $p = 2$).

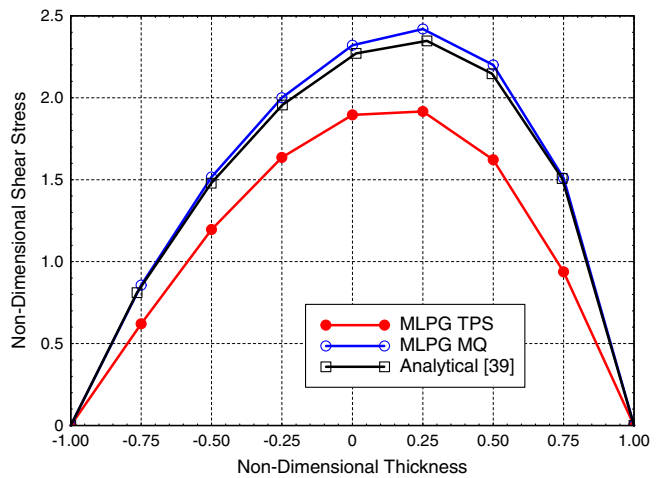


Fig. 8. Comparison of through-the-thickness distribution of the shear stress σ_{xz} at the plate edge $x = 0, y = b/2$ with that obtained from the analytical solution (SSSS square plate, pressure = $q_0 \sin \pi x/a \sin \pi y/a$, $V_c^- = 0$, $V_c^+ = 0.75$, $p = 2$).

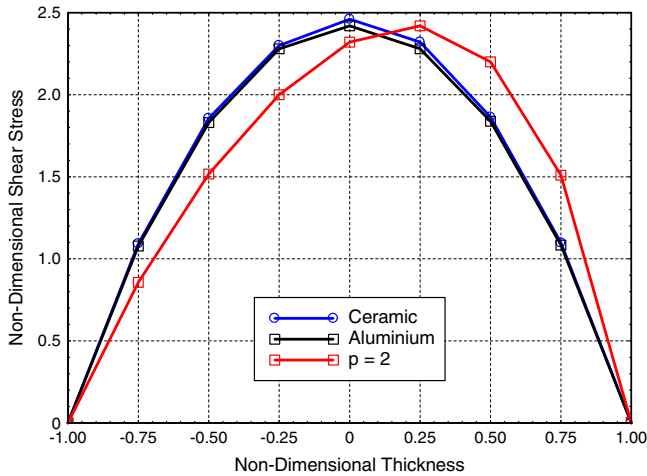
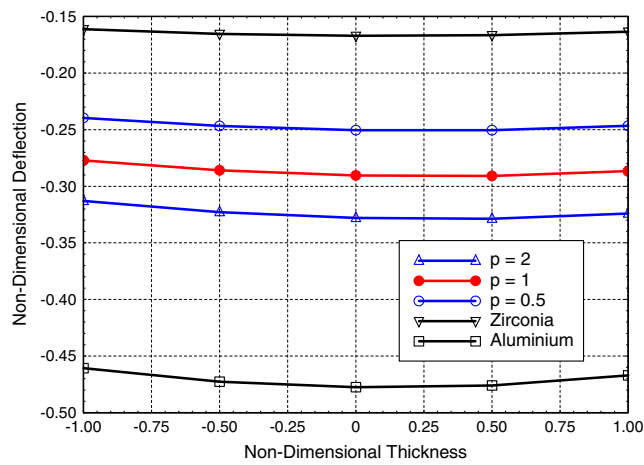
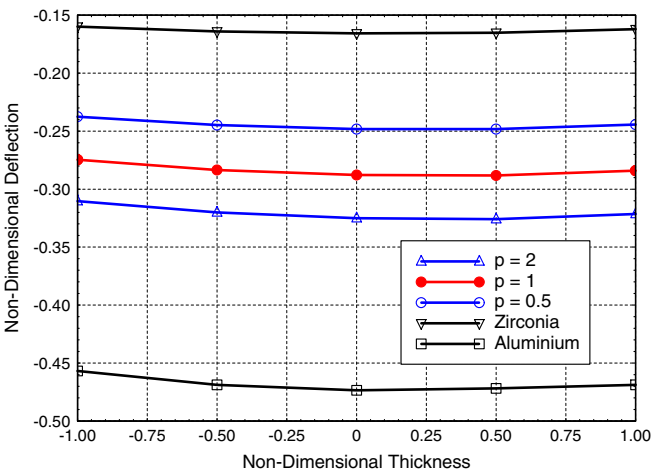


Fig. 9. Through-the-thickness distribution of the shear stress, σ_{xz} , at the plate edge $x=0, y=b/2$ for homogeneous aluminum, ceramic and FG plates (SSSS square plate, pressure = $q_0 \sin \pi x/a \sin \pi y/a$).



(a) MQ



(b) TPS

Fig. 10. For different values of the index p, deflection of points on the vertical line passing through the plate centroid (SSSS square plate, uniform pressure, $V_c^- = 0, V_c^+ = 1$).

ferent variables. As is common in solid mechanics, we set the body force field equal to zero.

In the figures and tables to follow, the vertical or the transverse displacement or the deflection w , the axial in-plane stress σ_{xx} , the transverse shear stress σ_{xz} , and the thickness co-ordinate z are non-dimensionalized as

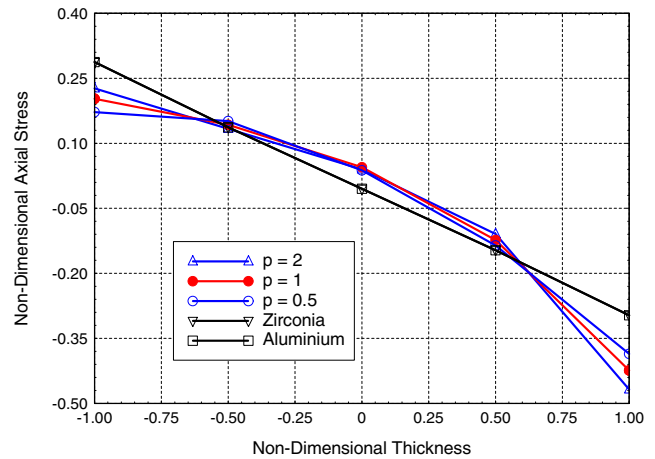
$$\bar{w} = \frac{100E_m t^3}{12a^4(1 - \nu_m^2)q_0} w, \quad \bar{\sigma}_{xx} = \frac{t^2}{q_0 a^2} \sigma_{xx},$$

$$\bar{z} = \frac{2z}{t}, \quad \bar{\sigma}_{xz} = \frac{10t}{q_0 a} \sigma_{xz} \quad (37)$$

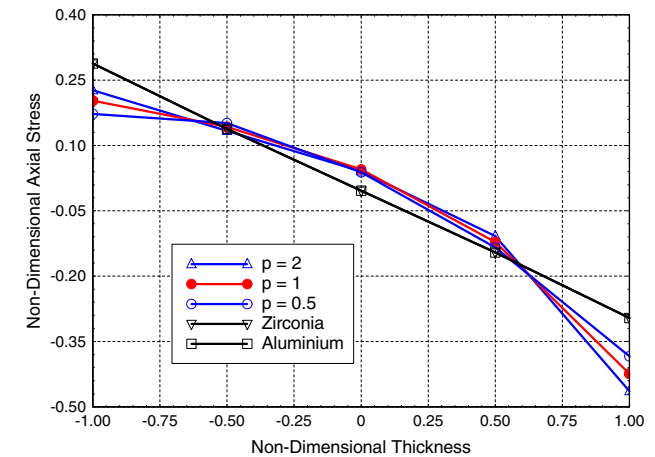
where a is the length of the side of a square plate, t the plate thickness, and q_0 is the magnitude of the normal traction on the top surface of the plate.

6.1. Comparison of numerical and analytical solutions

Computed centroidal deflection, axial in-plane stress at the center of the top surface, and through-the-thickness variation of the deflection, the axial stress at points on



(a) MQ



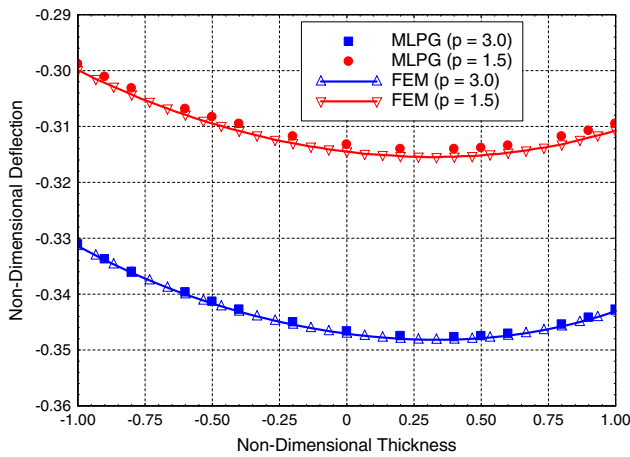
(b) TPS

Fig. 11. For different values of p, variation of the axial stress at points on the vertical line passing through the plate centroid (SSSS square plate, uniform pressure, $V_c^- = 0, V_c^+ = 1$).

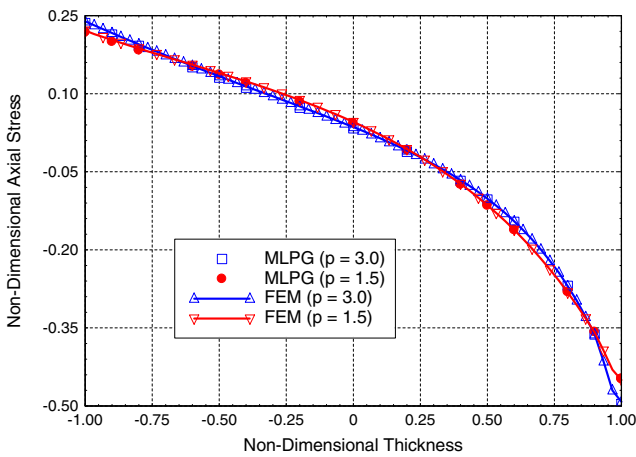
the vertical line passing through the centroid, and the transverse shear stress at points on the vertical line passing through the point $(0, a/2, 0)$ of a simply supported square Al/SiC square FG plate loaded on the top surface by the normal pressure $q_0 \sin \pi x/a \sin \pi y/a$ are compared in Figs. 4–7 with the corresponding results from the analytical solution of Vel and Batra [39]. It is clear from the plots of Figs. 4 and 5 that for $V_c^- = 0, V_c^+ = 1$ and different values of the index p in Eq. (36), the MQ and the TPS basis functions give centroidal deflections and the axial stress at the center of the top surface that are very close to those obtained analytically. However, as can be seen from results depicted in Fig. 6, for $V_c^- = 0, V_c^+ = 0.75$ and $p = 2$, deflections of points on the vertical line passing through the plate centroid computed with the MQ basis functions are closer to their analytical values than those obtained with the TPS basis functions; the maximum deviation from the analytical value of the computed deflection of any point on this line is $\sim 1\%$ for the TPS and $\sim 0.5\%$ for the MQ. Plots of the axial stress included in Figs. 5 and 7 imply that the axial stress

computed with the MQ and the TPS basis functions at every point on the vertical line passing through the plate centroid matches very well with that obtained from the analytical solution. Stresses computed from numerical solutions at points on plate boundaries usually have larger errors than those at interior points. We have compared in Fig. 8 values of the transverse shear stress, σ_{xz} , at points on the vertical line passing through the point $(0, a/2, 0)$ found from the analytical solution and the numerical solutions with MQ and TPS. The maximum errors in the transverse shear stress computed with the MQ and the TPS basis functions equal $\sim 4\%$ and 16% , respectively. This agrees with the observations in [44] for isotropic plates where the TPS basis functions were found to give accurate values of stresses at centers of different horizontal planes but not at points on the plate edges.

Because of the non-uniform composition of the material through the plate thickness, the maximum value of the transverse shear stress does not occur at a point on the midsurface as it does for an isotropic plate; e.g see Fig. 9.

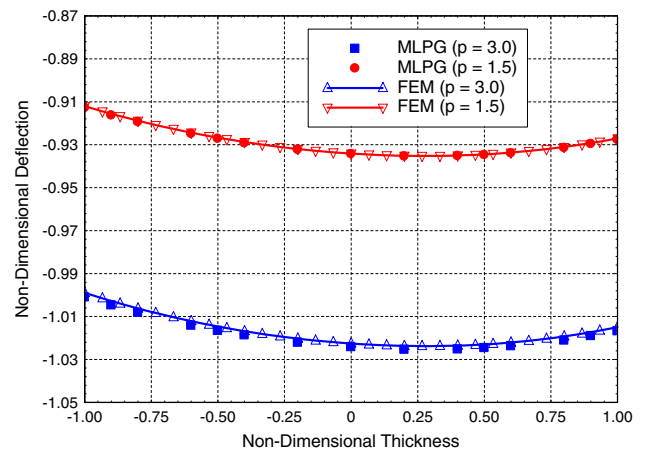


(a) Deflection

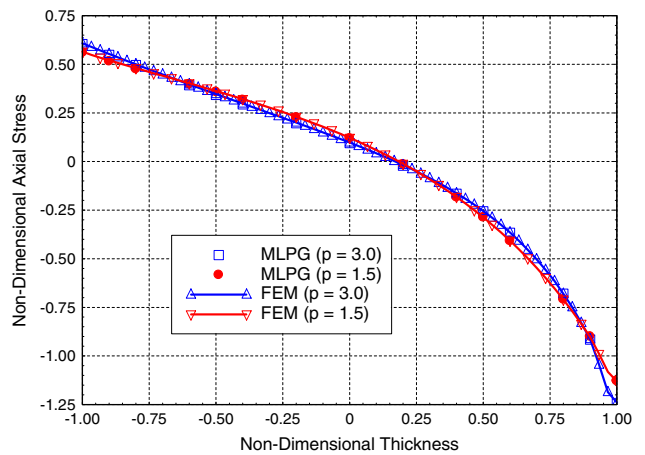


(b) Axial stress

Fig. 12. Comparison of MLPG MQ deflection and axial stress at points on the vertical line passing through the plate centroid with those computed by the finite element method (SSSS boundary condition, uniformly distributed pressure, $V_c^- = 0, V_c^+ = 1$).



(a) Deflection



(b) Axial stress

Fig. 13. Comparison of MLPG MQ deflection and axial stress at points on the vertical line passing through the plate centroid with those computed by the finite element method (SFSF boundary condition, uniformly distributed pressure, $V_c^- = 0, V_c^+ = 1$).

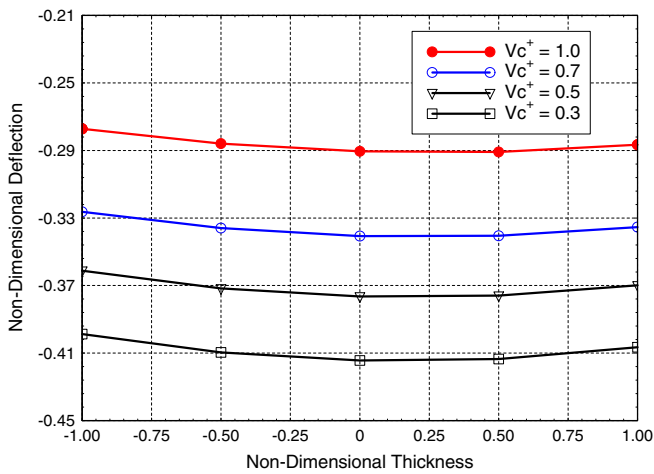
The location of the point of the maximum transverse shear stress is determined by the value of the index p in Eq. (36). We note that the magnitudes of the maximum shear stress for the aluminum and the FG plates are the same.

6.2. Results for an uniformly distributed pressure on the top surface of the plate

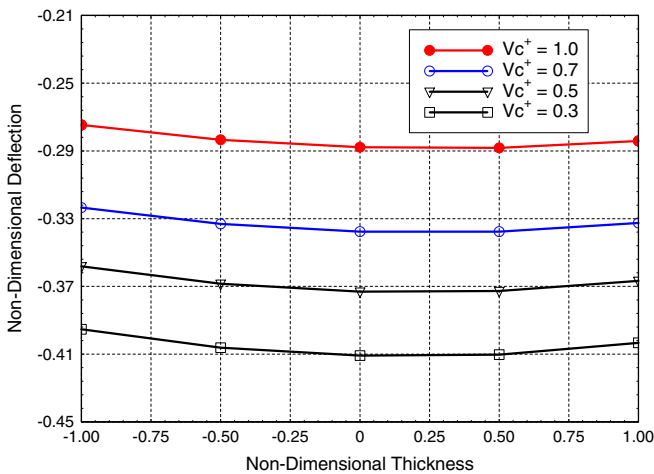
We have also studied deformations of a simply supported Al/ZrO₂ square plate loaded by an uniformly distributed pressure applied to its top surface. Figs. 10 and 11 show, respectively, the through-the-thickness distributions of the deflection and the stress at points on a vertical line passing through the plate centroid computed with both MQ and TPS RBFs. It can be seen that the addition of ZrO₂ to the Al plate reduces deflections since Young’s modulus of ZrO₂ is nearly three times that of Al. Furthermore, through-the-thickness distribution of the axial stress

becomes non-linear as opposed to being affine for a homogeneous material. Also, there is a reduction in the maximum tensile stress induced at points on the bottom surface of the plate and an increase in the maximum compressive stress at points on the top surface of the plate. Through-the-thickness distributions of the deflection and the axial stress for $p = 0.5, 1,$ and 2 are similar to each other and agree well with those given in Qian et al. [20] who used MLS basis functions. The MQ and TPS RBFs give very close values for both the deflection and the axial stress.

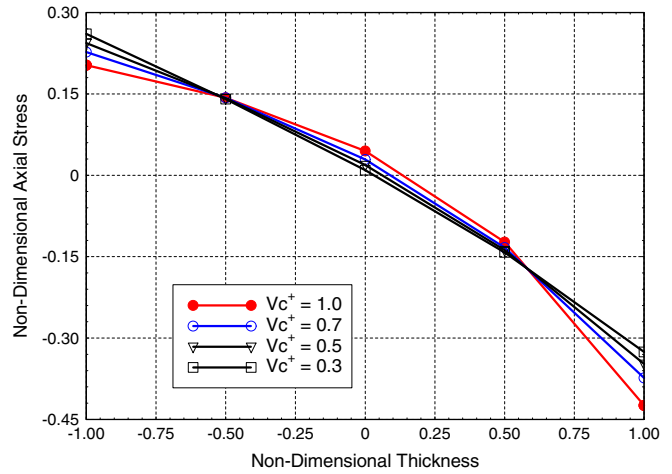
Through-the-thickness distributions of the deflection and the axial stress for a homogeneous plate are slightly asymmetric about the plate midsurface because of the asymmetry in the loads; the top surface has a uniformly distributed pressure acting on it while the bottom surface is traction free; this asymmetry was also found in the analytical solution of the problem.



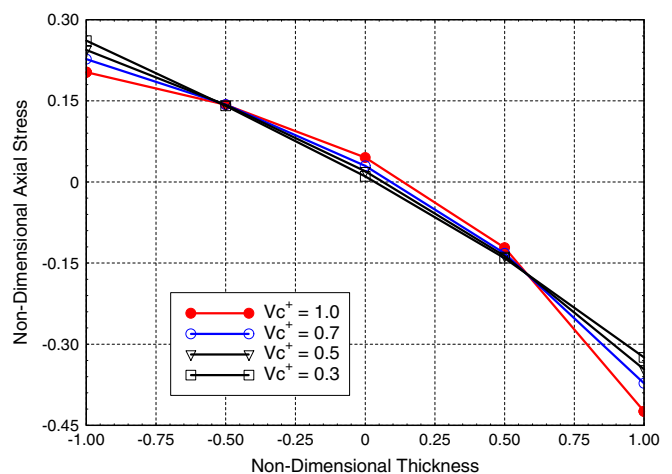
(a) MQ



(b) TPS



(a) MQ



(b) TPS

Fig. 14. For four values of the volume fraction of zirconia on plate’s top surface, deflection of points on the vertical line passing through the plate centroid (SSSS square plate, uniform pressure, $V_c^- = 0$).

Fig. 15. For four values of the volume fraction of zirconia on plate’s top surface, variation of the axial stress at points on the vertical line passing through the plate centroid (SSSS square plate, uniform pressure, $V_c^- = 0$).

6.2.1. Comparison with results from the three-dimensional analysis of the problem

We now provide validation of our results by comparing them with those obtained from the analysis of the three-dimensional problem by the finite element method (FEM). The FE mesh (12,000 solid elements in total) was created by using the commercial CAE code MSC Marc with 20 solid elements each in the x - and y -directions, and 30 elements in the thickness (z -) direction. Each one of the 30 layers in the thickness direction was assumed to be homogeneous with material properties (Young’s modulus and Poisson’s ratio) determined from Eqs. (33)–(36); thus the plate is assumed to be comprised of 30 layers of isotropic homogeneous materials perfectly bonded to each other. For $p = 1.5$ and 3.0 , with boundary conditions SSSS and SFSF, Figs. 12 and 13 show, respectively, the comparisons of the MQ-MLPG computed deflections and the axial stress (σ_{xx}) at points on the vertical line passing through the plate centroid with those obtained from the FEM. It can be seen that the MQ-MLPG results agree very well with those from the FEM. Similar excellent agreements

between results computed by the two methods were obtained for the CCCC and the SCSC plates; these results are omitted for the sake of brevity.

6.3. Effect of zirconia volume fraction variation

The effect of increasing the volume fraction, V_c^+ , of Zirconia in plate’s top surface on through-the-thickness distributions of the deflection and the axial stress is depicted in Figs. 14 and 15, respectively. With an increase in V_c^+ both the transverse deflection of a point and the axial tensile stress at a point on plate’s bottom surface decrease. However, the magnitude of the maximum compressive stress at a point on plate’s top surface increases with an increase in V_c^+ .

6.4. Effect of boundary conditions

Results for a square Al/ZrO₂ functionally graded plate with edges CCCC, SCSC, and SFSF and the results are given in Tables 3–8, and those a simply supported plate (SSSS) are included for comparison in Tables 1 and 2. For the boundary conditions considered, the MQ and

Table 1
Non-dimensional deflections at points on the vertical line passing through the centroid of a SSSS Al/ZrO₂ plate (uniformly distributed traction, $V_c^- = 0, V_c^+ = 1$)

\bar{z}	Aluminum	Zirconia	$p = 0.5$	$p = 1$	$p = 2$
<i>MQ, MLPGI</i>					
-1	-0.4607	-0.1613	-0.2396	-0.2771	-0.313
-0.5	-0.4726	-0.1654	-0.2468	-0.2859	-0.3229
0	-0.4775	-0.1671	-0.2505	-0.2905	-0.328
0.5	-0.4759	-0.1665	-0.2505	-0.2909	-0.3286
1	-0.4671	-0.1635	-0.2466	-0.2866	-0.3241
<i>TPS, MLPGI</i>					
-1	-0.4568	-0.1599	-0.2375	-0.2747	-0.3104
-0.5	-0.4687	-0.164	-0.2447	-0.2835	-0.32
0	-0.4734	-0.1657	-0.2482	-0.2878	-0.3251
0.5	-0.4718	-0.1652	-0.2482	-0.2882	-0.3259
1	-0.4687	-0.1622	-0.2443	-0.2841	-0.3214

Table 2
Non-dimensional axial stress at points on the vertical line passing through the centroid of a SSSS Al/ZrO₂ plate (uniformly distributed traction, $V_c^- = 0, V_c^+ = 1$)

\bar{z}	Aluminum	Zirconia	$p = 0.5$	$p = 1$	$p = 2$
<i>MQ, MLPGI</i>					
-1	0.2876	0.2876	0.172	0.2028	0.2268
-0.5	0.1372	0.1372	0.1512	0.1428	0.1336
0	-0.00472	-0.00472	0.0378	0.0448	0.03992
0.5	-0.1468	-0.1468	-0.1356	-0.1232	-0.1092
1	-0.2968	-0.2968	-0.3856	-0.424	-0.468
<i>TPS, MLPGI</i>					
-1	0.288	0.288	0.1724	0.2028	0.2268
-0.5	0.138	0.138	0.1512	0.1428	0.1336
0	-0.00389	-0.00389	0.0386	0.0452	0.0404
0.5	-0.1456	-0.1456	-0.134	-0.1216	-0.108
1	-0.296	-0.296	-0.384	-0.424	-0.464

Table 3
Non-dimensional deflection at points on the vertical line passing through the centroid of a CCCC Al/ZrO₂ plate (uniformly distributed traction, $V_c^- = 0, V_c^+ = 1$)

\bar{z}	Aluminum	Zirconia	$p = 0.5$	$p = 1$	$p = 2$
<i>MQ, MLPGI</i>					
-1	-0.2004	-0.0701	-0.1019	-0.1187	-0.1368
-0.5	-0.2061	-0.0722	-0.1054	-0.1229	-0.1416
0	-0.2088	-0.0731	-0.1073	-0.1253	-0.1444
0.5	-0.209	-0.0731	-0.1077	-0.126	-0.1454
1	-0.2059	-0.0721	-0.1063	-0.1244	-0.1437
<i>TPS, MLPGI</i>					
-1	-0.1997	-0.0699	-0.1015	-0.1182	-0.1362
-0.5	-0.2055	-0.0719	-0.105	-0.1224	-0.141
0	-0.2082	-0.0729	-0.1069	-0.1248	-0.1438
0.5	-0.2082	-0.0729	-0.1073	-0.1255	-0.1447
1	-0.2051	-0.0718	-0.1058	-0.1239	-0.143

Table 4
Non-dimensional axial stress at the points on the vertical line passing through the centroid of a CCCC Al/ZrO₂ plate (uniformly distributed traction, $V_c^- = 0, V_c^+ = 1$)

\bar{z}	Aluminum	Zirconia	$p = 0.5$	$p = 1$	$p = 2$
<i>MQ, MLPGI</i>					
-1	0.1432	0.1432	0.0844	0.0992	0.1116
-0.5	0.0636	0.0636	0.0712	0.0668	0.0624
0	-0.00804	-0.00804	0.01412	0.01788	0.01564
0.5	-0.0796	-0.0796	-0.0732	-0.0664	-0.0592
1	-0.1592	-0.1592	-0.2044	-0.2252	-0.248
<i>TPS, MLPGI</i>					
-1	0.1428	0.1428	0.0848	0.0992	0.1112
-0.5	0.0636	0.0636	0.0708	0.0668	0.062
0	-0.00808	-0.00808	0.01412	0.01792	0.0156
0.5	-0.0796	-0.0796	-0.0728	-0.0664	-0.0592
1	-0.1588	-0.1588	-0.2036	-0.2244	-0.2464

TPS RBFs give very close values of deflections and axial stresses at points on the vertical line passing through the plate centroid. A comparison of results in Tables 1, 3, 5, and 7 reveals that both the magnitude of the deflection

Table 5
Non-dimensional deflection at points on the vertical line passing through the centroid of a SCSC Al/ZrO₂ plate (uniformly distributed traction, $V_c^- = 0, V_c^+ = 1$)

\bar{z}	Aluminum	Zirconia	$p = 0.5$	$p = 1$	$p = 2$
<i>MQ, MLPGI</i>					
-1	-0.2794	-0.0977	-0.143	-0.1664	-0.1909
-0.5	-0.2872	-0.1005	-0.1477	-0.1721	-0.1973
0	-0.2905	-0.1017	-0.1501	-0.1751	-0.2008
0.5	-0.2903	-0.1016	-0.1505	-0.1758	-0.2018
1	-0.2855	-0.0999	-0.1483	-0.1734	-0.1993
<i>TPS, MLPGI</i>					
-1	-0.2771	-0.097	-0.1419	-0.1651	-0.1894
-0.5	-0.2849	-0.01	-0.1465	-0.1707	-0.1957
0	-0.2882	-0.1009	-0.1489	-0.1737	-0.1993
0.5	-0.288	-0.1008	-0.1492	-0.1743	-0.2002
1	-0.2833	-0.0991	-0.1472	-0.172	-0.1977

Table 6
Non-dimensional axial stress at points on the vertical line passing through the centroid of a SCSC Al/ZrO₂ plate (uniformly distributed traction, $V_c^- = 0, V_c^+ = 1$)

\bar{z}	Aluminum	Zirconia	$p = 0.5$	$p = 1$	$p = 2$
<i>MQ, MLPGI</i>					
-1	0.1796	0.1796	0.1052	0.1244	0.1408
-0.5	0.0856	0.0856	0.092	0.0872	0.0824
0	-0.002688	-0.002688	0.02316	0.02728	0.02444
0.5	-0.0908	-0.0908	-0.0824	-0.0752	-0.0672
1	-0.1848	-0.1848	-0.2356	-0.2604	-0.2884
<i>TPS, MLPGI</i>					
-1	0.178	0.178	0.1044	0.1232	0.1396
-0.5	0.0848	0.0848	0.0912	0.0864	0.0816
0	-0.002784	-0.002784	0.02288	0.02696	0.02412
0.5	-0.0904	-0.0904	-0.082	-0.0744	-0.0668
1	-0.1832	-0.1832	-0.2336	-0.2576	-0.2852

Table 7
Non-dimensional deflection at points on the vertical line passing through the centroid of a SFSF Al/ZrO₂ plate (uniformly distributed traction, $V_c^- = 0, V_c^+ = 1$)

\bar{z}	Aluminum	Zirconia	$p = 0.5$	$p = 1$	$p = 2$
<i>MQ MLPGI</i>					
-1	-1.4092	-0.4931	-0.7378	-0.8509	-0.9518
-0.5	-1.4273	-0.4995	-0.7489	-0.8642	-0.9668
0	-1.4345	-0.5019	-0.7543	-0.8708	-0.9744
0.5	-1.4308	-0.5007	-0.7538	-0.8708	-0.9748
1	-1.4162	-0.4956	-0.7473	-0.8638	-0.9672
<i>TPS MLPGI</i>					
-1	-1.4086	-0.4929	-0.7376	-0.8501	-0.9502
-0.5	-1.4261	-0.4991	-0.7483	-0.8630	-0.9645
0	-1.4330	-0.5015	-0.7532	-0.8693	-0.9719
0.5	-1.4295	-0.5003	-0.7530	-0.8693	-0.9723
1	-1.4156	-0.4954	-0.7469	-0.8628	-0.9651

Table 8
Non-dimensional axial stress at points on the vertical line passing through the centroid of a SFSF Al/ZrO₂ plate (uniformly distributed traction, $V_c^- = 0, V_c^+ = 1$)

\bar{z}	Aluminum	Zirconia	$p = 0.5$	$p = 1$	$p = 2$
<i>MQ MLPGI</i>					
-1	0.7360	0.7360	0.4400	0.5200	0.5840
-0.5	0.3604	0.3604	0.3968	0.3748	0.3496
0	-0.0028	-0.0028	0.1056	0.1232	0.1108
0.5	-0.3660	-0.3660	-0.3396	-0.3084	-0.2724
1	-0.7440	-0.7440	-0.9680	-1.0680	-1.176
<i>TPS MLPGI</i>					
-1	0.7280	0.7280	0.4360	0.5160	0.5760
-0.5	0.3568	0.3568	0.3928	0.3708	0.3460
0	-0.0031	-0.0031	0.1040	0.1212	0.1092
0.5	-0.3632	-0.3632	-0.3368	-0.3060	-0.2704
1	-0.7360	-0.7360	-0.9600	-1.0560	-1.1600

and the axial stress at the center of a horizontal plane decrease with a change in boundary conditions from SFSF to SSSS, SSSS to SCSC, and SCSC to CCCC. The magnitudes of the deflection and the axial stress at the center of a horizontal surface for a clamped plate are about one-half of those for the corresponding simply supported plate. The deflections for the SFSF plate are about three times as much as the simply supported plate. The MQ and the TPS RBFs give results that are very close to each other for all boundary conditions examined.

7. Conclusions

A higher order shear and normal deformable plate theory (HOSNDPT) has been combined with the Meshless Local Petrov-Galerkin (MLPG) method to analyze static deformations of functionally graded thick plates. The MLPG method employs suitably located nodes in the problem domain and does not require a mesh for either interpolation of the trial solution or numerical evaluation of integrals appearing in the weak formulation of the problem. The Multiquadric and Thin Plate Spline radial basis functions have been used for approximating the trial solution and a fourth-order spline weight function for the test function. The RBF shape functions satisfy the delta function property and thus no special technique is needed to impose essential boundary conditions. Governing equations in the HOSNDPT are second-order partial differential equations, and traction boundary conditions on plate's top and bottom surfaces are exactly satisfied.

The plate material is comprised of two isotropic constituents, and its macroscopic response is assumed to be isotropic. The effective material properties are determined using the Mori-Tanaka homogenization technique. For a simply supported square plate, through-the-thickness distributions of the deflection and the axial stress are found to agree very well with those found from the analytical solution of Vel and Batra [39]. Also, for a plate with two opposite edges free and the other two simply supported, computed results are in excellent agreement with those

obtained by analyzing three-dimensional deformations of the plate by the finite element method. For all types of boundary conditions, presently computed results match well with those obtained by Qian et al. [20] who used basis functions derived by the moving least squares approximation and modified the stiffness matrix and the load vector to exactly satisfy essential boundary conditions. The present implementation of the MLPG with RBFs is computationally less expensive as compared to the MLS scheme, and yields equally accurate results. The MQ and TPS RBFs give equally good results. However, for through-the-thickness variation of the transverse shear stress at points on the edge of a simply supported plate, the maximum deviations in the computed stress with MQ and RBFs from the analytical values are 4% and 16%, respectively. The centroidal deflection of a thick clamped square plate is nearly one-fourth of that of a simply supported plate, about one-seventh of a plate with two opposite edges simply supported and the other two free, and about two-third of a plate with two opposite edges simply supported and the other two clamped. The axial tensile stress at the center of the bottom surface of a clamped plate is about one-half of that of a simply supported plate, one-fifth of that when two opposite edges are simply supported and the other two are free, and 8–10th of that when two opposite edges are simply supported and the other two are clamped.

Acknowledgements

DFG acknowledges the support of the Irish Research Council for Science, Engineering and Technology Postgraduate Scholarship scheme to the University of Limerick, and the Internship from University of Delaware Center for Composite Materials. RCB's work was partially supported by the ONR Grant N00014-1-98-0300 to Virginia Polytechnic Institute and State University with Dr. Y.D.S. Rajapakse as the program manager.

References

- [1] Berger R, Kwon P, Dharan CKH. High speed centrifugal casting of metal matrix composites. In: The fifth international symposium on transport phenomena and dynamics of rotating machinery, Maui, Hawaii, May 8–11; 1994.
- [2] Fukui Y. Fundamental investigation of functionally gradient materials manufacturing system using centrifugal force. *JSME Int J Ser III* 1991;34:144–8.
- [3] Choy K-L, Felix E. Functionally graded diamond like carbon coatings on metallic substrates. *Mater Sci Eng A* 2000;278:162–9.
- [4] Khor KA, Gu YW. Effects of residual stress on the performance of plasma sprayed functionally graded $ZrO_2/NiCoCrAlY$ coatings. *Mater Sci Eng A* 2000;277:64–76.
- [5] Lambros A, Narayanaswamy A, Santare MH, Anlas G. Manufacturing and testing of a functionally graded material. *J Eng Mater Technol* 1999;121:488–93.
- [6] Braval E, Aghahanian K, Luszcz SJ. Microstructure and composition of alumina/aluminum composites made by the directed oxidation of aluminum. *J Am Ceram Soc* 1990;73:2610–4.
- [7] Manor E, Ni H, Levi CG, Mehrabian R. Microstructure evaluation of $SiC/Al_2O_3/Al$ alloy composite produced by melt oxidation. *J Am Ceram Soc* 1993;26:1777–87.
- [8] Lo KH, Christensen RM, Wu EM. A high-order theory of plate deformation. *J Appl Mech* 1997;44:663–76.
- [9] Phan ND, Reddy JN. Analysis of laminated composite plates using a higher-order shear deformation theory. *Int J Num Methods Eng* 1985;21:2201–19.
- [10] Batra RC, Vidoli S. Higher-order piezoelectric plate theory derived from a three-dimensional variational principle. *AIAA J* 2002;40:91–104.
- [11] Kocak S, Hassis H. A higher order shear deformable finite element for homogeneous plates. *Eng Struct* 2003;25:131–9.
- [12] Reddy JN. Analysis of functionally graded plates. *Int J Numer Meth Eng* 2000;47:663–84.
- [13] Cheng ZQ, Batra RC. Deflection relationships between the homogeneous Kirchhoff plate theory and different functionally graded plate theories. *Arch Mech* 2000;52:143–58.
- [14] Cheng ZQ, Batra RC. Exact correspondence between eigenvalues of membranes and functionally graded simply supported polygonal plates. *J Sound Vib* 2000;229:879–95.
- [15] Cheng ZQ, Batra RC. Three-dimensional thermoelastic deformations of a functionally graded elliptic plate. *Compos: Part B* 2000;31:97–106.
- [16] Loy CT, Lam KY, Reddy JN. Vibrations of functionally graded cylindrical shells. *Int J Mech Sci* 1999;41:309–24.
- [17] Batra RC, Vidoli S, Vestroni F. Plane wave solutions and modal analysis in higher order shear and normal deformable plate theories. *J Sound Vib* 2002;257:63–88.
- [18] Batra RC, Aimmancee S. Vibrations of thick isotropic plates with higher order shear and normal deformable plate theories. *Comput Struct* 2005;83:934–55.
- [19] Qian LF, Batra RC, Chen LM. Elastostatic deformations of a thick plate by using a higher-order shear and normal deformable plate theory and two meshless local Petrov–Galerkin (MLPG) methods. *Comput Model Eng Sci* 2003;4:161–76.
- [20] Qian LF, Batra RC, Chen LM. Static and dynamic deformations of thick functionally graded elastic plate by using higher-order shear and normal deformable plate theory and meshless local Petrov–Galerkin method. *Compos: Part B* 2004;35:685–97.
- [21] Qian LF, Batra RC. Transient thermoelastic deformations of a thick functionally graded plate. *J Therm Stresses* 2004;27:705–40.
- [22] Belytschko T, Lu YY, Gu L. Element-free Galerkin methods. *Int J Num Meth Eng* 1994;37:229–56.
- [23] Liu WK, Jun S, Zhang Y. Reproducing kernel particle methods. *Int J Num Meth Fluids* 1995;20:1081–106.
- [24] Duarte CA, Oden JT. An h-p adaptive method using clouds. *Comput Meth Appl Mech Eng* 1996;139:237–62.
- [25] Babuska I, Melenk J. The partition of unity method. *Int J Num Meth Eng* 1997;40:727–58.
- [26] Atluri SN, Zhu T. A new meshless local Petrov–Galerkin (MLPG) approach in computational mechanics. *Comput Mech* 1998;22:117–27.
- [27] Atluri SN, Shen S. The meshless local Petrov–Galerkin (MLPG) method. Tech Science Press; 2002.
- [28] Hardy RL. Multiquadric equations of topography and other irregular surfaces. *J Geophys Res* 1971;76:1905–15.
- [29] Kansa EJ. Multiquadrics – A scattered data approximation scheme with application to computational fluid-dynamics – I and II. *Comput Math Appl* 1990;19:127–61.
- [30] Golberg MA, Chen CS, Karur SR. Improved multiquadric approximation for partial differential equations. *Eng Anal Bound Elem* 1996;18:9–17.
- [31] Fasshauer GE. Solving partial differential equations by collocation with radial basis functions. In: Le M haut A, Rabut C, Schumaker LL, editors. Surface fitting and multiresolution methods. Nashville TN: Vanderbilt University Press; 1997. p. 131–8.
- [32] Wendland H. Meshless Galerkin method using radial basis functions. *Math Comput* 1999;68:1521–31.

- [33] Liu GR, Gu YT. A local radial point interpolation method (LRPIM) for free vibration analysis of 2D solids. *J Sound Vib* 2001;246: 29–46.
- [34] Wang JG, Liu GR. On the optimal shape parameters of radial basis functions used for 2D meshless methods. *Comput Methods Appl Mech Eng* 2002;191:2611–30.
- [35] Xiao JR, McCarthy MA. A local Heaviside weighted meshless method for two-dimensional solids using radial basis functions. *Comput Mech* 2003;31:301–15.
- [36] Xiao JR, Gama BA, Gillespie Jr JW, Kansa EJ. Meshless solutions of 2D contact problems by subdomain variational inequality and MLPG method with radial basis functions. *Eng Anal Bound Elem* 2005;29:95–106.
- [37] Ferreira AJM, Batra RC, Roque CMC, Qian LF, Martins PALS. Static analysis of functionally graded plates using third-order shear deformation theory and a meshless method. *Compos Struct* 2005;69:449–57.
- [38] Mori T, Tanaka K. Average stress in matrix and average elastic energy of materials with misfitting inclusions. *Acta Metall* 1973;21:571–4.
- [39] Vel SS, Batra RC. Exact solution for thermoelastic deformations of functionally graded thick rectangular plates. *AIAA J* 2002;40:1421–33.
- [40] Frohlich H, Sack R. Theory of the rheological properties of dispersions. *Proc R Soc* 1946;A185:415–30.
- [41] Hill R. A self-consistent mechanics of composite materials. *J Mech Phys Solids* 1965;13:213–22.
- [42] Jiang B, Batra RC. Effective properties of a piezocomposite containing shape memory alloy and inert inclusions. *Continuum Mech Therm* 2002;14:87–111.
- [43] Vel SS, Batra RC. Three-dimensional thermoelastic analysis of transient thermal stresses in functionally graded plates. *Int J Solids Struct* 2003;40:7181–96.
- [44] Vel SS, Batra RC. Three-dimensional exact solution for the vibration of functionally graded rectangular plates. *J Sound Vib* 2004;272: 703–30.
- [45] Xiao JR, Batra RC, Gilhooley DF, Gillespie Jr JW, McCarthy MA. Bending analysis of thick plates by using a higher-order shear and normal deformable plate theory and MLPG method with radial basis functions. *Comput Meth Appl Mech Eng*, in press.